Wireless Power Transfer, 2018, 5(1), 20–26. © Cambridge University Press, 2017
doi:10.1017/wpt.2017.18

SPECIAL ISSUE ON CONTACTLESS CHARGING FOR ELECTRIC VEHICLES

Contactless power transfer system for sealed lead acid battery charging

GAUTAM RITURAJ, BRIJESH KUMAR KUSHWAHA AND PRAVEEN KUMAR

In this paper, an experimental study is carried out while charging the sealed lead acid battery bank using a series-parallel (SP) compensated contactless power transfer (CPT) system. Constant current (CC) and constant voltage (CV) modes are used for charging the battery bank. An expression of optimum operating frequency is derived to maintain the maximum compensated coil efficiency throughout the load variation in charging process. An experimental setup of SP compensated CPT system is built for charging the battery bank. The variation of compensated coil efficiency and the load phase angle with respect to different operating frequencies in CC and CV modes is verified with the measurement. Based on the analysis, the control parameters are identified.

Keywords: Battery charging, Contactless power transfer system, Maximum efficiency, Optimum operating frequency, SP compensation

Received 30 April 2017; Revised 4 November 2017; Accepted 6 November 2017; first published online 29 November 2017

I. INTRODUCTION

Contactless power transfer (CPT) is gaining more popularity in recent years due to its safer and convenient operation compared with the plug-in charger for electric vehicles [1–5]. Contactless coils play a vital role to transfer the power in the CPT system. The air core contactless coils have large leakage inductance, which needs to be compensated for an efficient power transfer. Generally, the leakage inductance of contactless coils is compensated by using the capacitor compensation technique (CCT) [6]. Based on the CCT, four compensation topologies are used in the CPT system [6, 7]. Among the four compensation topologies, series-series (SS) and series-parallel (SP) compensation topologies are widely used for charging the battery [8].

For SS and SP compensations, a comparative study in terms of efficiency, load, and frequency control technique is reported in [9]. Authors have found that SS compensation topology is the best due to its peak efficiency and the fixed frequency control scheme. In [10], the experimental comparison for various operating frequencies, different loads, various distance, and efficiency of SS and SP topologies is reported. The design of parameter values, analysis of the bifurcation frequencies, and corresponding output power for SP compensated inductive power transfer system are given in [11]. For SS compensated inductive charging system, an adaptive frequency control technique is used to achieve a zero voltage switching (ZVS) throughout the charging process, which is reported in [12]. For SP compensated CPT system with a resistive load, a frequency tracking control method is explained in [13]. Very few works have used the battery as a load in the CPT system, which are reported in [5, 14–16]. The work on the design and control scheme for charging of the lithium iron phosphate battery using the CPT system is presented in [14]. The variable frequency control for SS compensated CPT system with an electronic load and battery is reported in [5, 15]. In [15], a closed loop scheme with the proportional-integral controller for constant current (CC) and constant voltage (CV) charging is also presented. The design of wireless power transfer battery charger for electric city car using SS compensation with the battery charging profile and the circular spiral coil is presented in [16].

Generally, at the resonant frequency and no load condition (secondary open), for SS compensation topology, the current in primary side can increase to a very high value [17]. However, in case of SP compensation topology, the current does not increase to a very high value [17]. Thus, in this work, SP compensation topology is chosen for charging the battery bank.

In this paper, the experimental discussion during charging of the lead acid battery bank in CC and CV modes using the SP compensated CPT system is presented and the control parameters are also identified. The measured charging profile of the lead acid battery bank in CC and CV modes is presented. In addition, an expression of optimum operating frequency is derived to get the maximum compensated coil efficiency throughout the charging process. The calculated optimum operating frequency also maintains the ZVS during the charging process.

The rest of the paper is organized as follows: Section II presents the system details and the governing equations. The

Department of Electronics and Electrical Engineering, Indian Institute of Technology Guwahati, Guwahati – 781039, Assam, India
Corresponding author: G. Rituraj
Email: g.rituraj@iitg.ernet.in

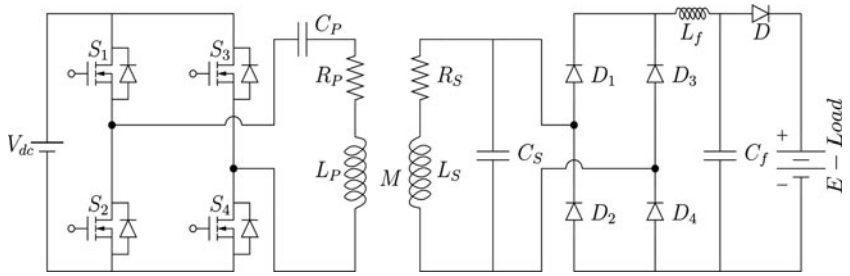

Fig. 1. Schematic of contactless charging system with SP compensation.

experimental setup description and observations are presented in Section III. Finally, the conclusions are given in Section IV.

II. SP COMPENSATED CPT SYSTEM

A) Contactless charging system

The circuit diagram of contactless charging system with SP compensation is depicted in Fig. 1. A DC voltage source V_{dc} is applied to the input of H-bridge inverter. For the experiment purpose, a variable DC source is used to keep the current and voltage constant during charging of the battery bank in CC and CV modes, respectively.

The compensated primary coil is excited with high-frequency current, generated by the high-frequency H-bridge inverter. On the secondary side, a parallel compensated coil is connected with a diode bridge rectifier, which converts high-frequency AC voltage to DC voltage. In order to get pure DC voltage and current, LC filter is used. Diode D ensures charging of the battery bank only when the anode voltage is greater than the cathode voltage. The battery bank is represented as E-Load. The symbols R_P and R_S denote AC resistance of the primary and secondary coils, respectively.

The primary and secondary compensation capacitors C_P and C_S are calculated at resonance frequency ω_o, using (1) and (2), respectively [6, 8, 9, 13].

$$C_P = \frac{1}{\omega_o^2(L_P - (M^2/L_S))}, \tag{1}$$

$$C_S = \frac{1}{\omega_o^2 L_S}, \tag{2}$$

where L_P and L_S represent the primary and secondary self-inductances, respectively.

B) Equivalent model of the charging system

An equivalent circuit model of the charging system is shown in Fig. 2 [18]. The relation between coupling coefficient k and mutual inductance M is given in (3).

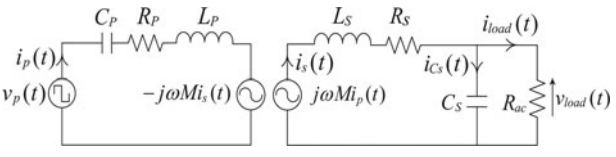

Fig. 2. Equivalent circuit model of the SP compensated CPT system.

$$k = \frac{M}{\sqrt{L_P L_S}}, \tag{3}$$

$$Z_P = R_P + j\left(h\omega L_P - \frac{1}{h\omega C_P}\right), \tag{4}$$

$$Z_r = \frac{(h\omega M)^2}{R_S + jh\omega L_S + \left(R_{ac}/(1 + jh\omega C_S R_{ac})\right)}, \tag{5}$$

$$R_{ac} = \frac{\pi^2}{8} R_L, \tag{6}$$

$$Z_T = R_P + j\left(h\omega L_P - \frac{1}{h\omega C_P}\right) + \frac{(h\omega M)^2}{R_S + jh\omega L_S + \left((R_{ac}/1 + jh\omega C_S R_{ac})\right)}. \tag{7}$$

For (4)–(7), Z_P, Z_r, Z_T represent the primary side, reflected, and total impedances of the CPT system for h^{th} harmonic, respectively. R_{ac} is the effective load resistance, seen from the input side of the rectifier. R_L is the equivalent load resistance of the battery bank, which depends on charging status of battery voltage and current [15].

The Fourier series expressions of the primary instantaneous voltage $v_p(t)$ (inverter output) and current $i_p(t)$ are given in (8) and (9), respectively.

$$v_p(t) = \sum_{h=1,3,5..}^{\infty} \frac{4V_{dc}}{\pi h} \sin h\omega t, \tag{8}$$

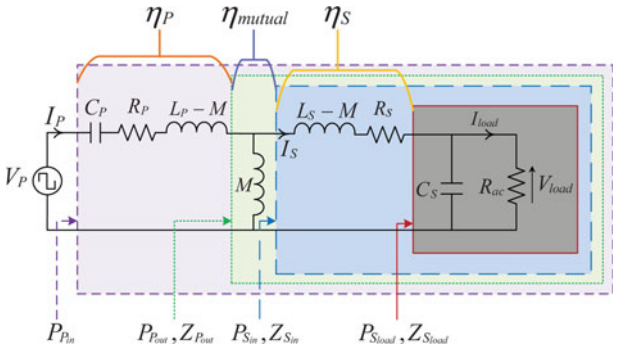

Fig. 3. AC equivalent circuit based on T-model of contactless coils for SP compensated CPT system.

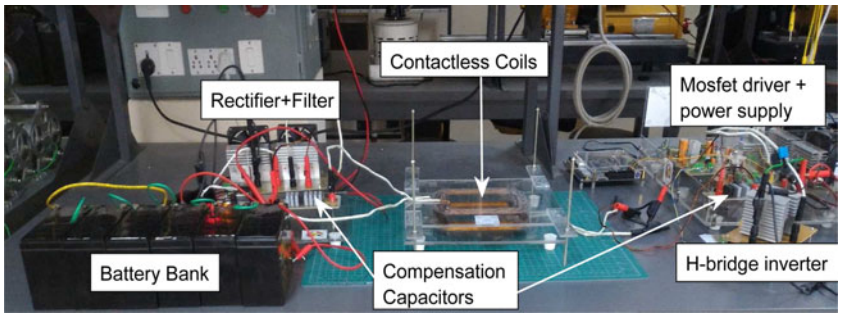

Fig. 4. Laboratory view of the experimental setup.

$$i_p(t) = \sum_{h=1,3,5..}^{\infty} \frac{4V_{dc}}{\pi h|Z_T|}\sin(h\omega t - \theta_{Z_T}), \tag{9}$$

where θ_{Z_T} is the load phase angle of total impedance Z_T, seen from the output of H-bridge inverter.

The compensated coil (transmission) efficiency η_{cc} of the SP compensated CPT system is calculated using AC equivalent circuit based on T-model of contactless coils, as shown in Fig. 3. Equivalent series resistance of C_P and C_S are not considered in the efficiency calculation due to its insignificant effect. Hence, the real power consumed in capacitor is zero, and the η_{cc} of the SP compensated CPT system is given as

$$\eta_{cc} = \eta_P \cdot \eta_{mutual} \cdot \eta_S, \tag{10}$$

where η_P, η_{mutual}, and η_S are the efficiencies of the equivalent primary, mutual, and secondary of the system, respectively. Since the mutual has only a reactive component, the active power consumed is zero ($\eta_{mutual} = 1$). From Fig. 3, $\eta_P = P_{P_{out}}/P_{P_{in}}$ and $\eta_S = P_{S_{load}}/P_{S_{in}}$, where the input power $P_{P_{in}} = (P_{P_{out}} + \text{loss in } R_P)$ and $P_{S_{in}} = (P_{S_{load}} + \text{loss in } R_S)$. Therefore, the expression (10) can be written as

$$\eta_{cc} = \frac{\Re(Z_{P_{out}})}{\Re(Z_{P_{out}}) + R_P} \cdot 1 \cdot \frac{\Re(Z_{S_{load}})}{\Re(Z_{S_{load}}) + R_S}, \tag{11}$$

where the symbol $\Re$ represents the real part of the respective impedances, $Z_{S_{load}} = R_{ac}/(1 + j\omega C_S R_{ac})$, and $Z_{P_{out}} = j\omega M Z_{S_{in}}/(j\omega M + Z_{S_{in}})$. By substituting $Z_{S_{load}}$ and $Z_{P_{out}}$ in (11), the final expression of η_{cc} is given as

$$\eta_{cc} = \frac{M^2\omega^2 R_{ac}}{(C_S^2 R_{ac}^2(L_S^2 R_P + M^2 R_S)\omega^4 + A\omega^2 + R_P(R_S^2 + 2R_S R_{ac} + R_{ac}^2)}, \tag{12}$$

where $A = (((C_S^2 R_S^2 - 2C_S L_S)R_{ac}^2 + L_S^2)R_P + M^2(R_S + R_{ac}))$ and $\omega = 2\pi f$.

Table 1. Specifications of power components and battery bank.

Specification	Value
Power MOSFETs in inverter	IRFP460
Hyperfast diodes in rectifier	RHRP30120
Half bridge gate driver IC	IR2110
Sealed lead acid battery 7.2 Ah	12 × 6 V

From (12), the optimum operating frequency ($f_{optimum}$), at which the maximum η_{cc} is achieved, can be obtained by (13) and is given in (14).

$$\left.\frac{\partial \eta_{cc}}{\partial f}\right|_{f_{optimum}} = 0, \tag{13}$$

$$f_{optimum} = \frac{1}{2\pi}\frac{R_P^{1/4}\sqrt{R_S + R_{ac}}}{\sqrt{R_{ac}C_S}(L_S^2 R_P + M^2 R_S)^{1/4}}. \tag{14}$$

III. EXPERIMENTAL DISCUSSION

Figure 4 shows the laboratory view of real-time implementation for charging the battery bank using SP compensated CPT system. Six number of sealed maintenance-free lead acid batteries connected in series are used as a battery bank in the experiment. However, the other technologies of batteries like lithium, sodium, etc. can also be used. The details of power switches and the battery bank used in CPT system are provided in Table 1. The primary and secondary coils are made using Litz wire, having American wire gauge #32 copper wire. The vertical distance between primary and secondary coils can be adjusted up to 10 cm, while in the experiment it is kept at 2 cm. A resonance frequency of 197.60 kHz is selected for the SP compensated CPT system. To vary the output frequency of H-bridge inverter, a pulse width modulation controller IC SG3525A is used. The remaining specifications of the SP compensated CPT system are given in the Table 2.

The charging of lead acid battery bank is performed in open loop (by manually controlling the input DC voltage to maintain CC and CV modes) at the resonance frequency. The measured charging profile and the equivalent resistance

Table 2. Specifications of the SP compensated CPT system.

Symbol	Parameter	Value
N_P	Primary number of turns	11
N_S	Secondary number of turns	11
L_P	Primary self-inductance	29.73 μH
L_S	Secondary self-inductance	30.07 μH
R_P	AC resistance of the primary coil at 200 kHZ	0.133 Ω
R_S	AC resistance of the secondary coil at 200 kHz	0.137 Ω
k	Coupling coefficient at 2 cm air gap	0.51
C_P	Primary compensation capacitor	29.11 nF
C_S	Secondary compensation capacitor	21.51 nF
f_o	Resonance frequency	197.60 kHz

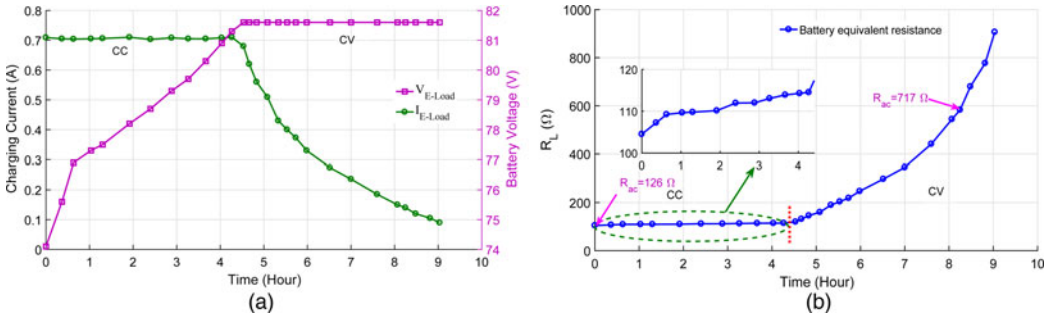

Fig. 5. (a) Measured charging profile and (b) equivalent resistance profile of a lead acid battery bank at the resonance frequency.

profile of a lead acid battery bank are shown in Fig. 5. The initial voltage of the battery bank is 74.1 V, which is first charged in CC mode for about 4 h, then in CV mode for about 5 h, as shown in Fig. 5(a). The charging current in CC mode is set to a constant 700 mA. Whereas, in CV mode, the voltage across the battery is maintained at 81.6 V by decreasing the input DC voltage. This results in a decrease in the charging current. The equivalent resistance profile of battery bank, as shown in Fig. 5(b), is obtained from Fig. 5(a).

In Fig. 6, the variation of compensated coil efficiency, calculated from (12), with respect to (w.r.t.) different operating frequencies (0–500 kHz) for $R_{ac} = 126\ \Omega$ and $717\ \Omega$, is given. Two cases for the variation in compensated coil efficiency are presented in Fig. 6. One is for the CC mode ($R_{ac} = 126\ \Omega$) and another is for the CV mode ($R_{ac} = 717\ \Omega$). For both the cases in Fig. 6, the maximum compensated coil efficiency ($\eta_{cc_{max}}$) is shown by zooming the dotted circle area. From the zoomed version, it can be seen that $\eta_{cc_{max}}$ lies on the left side of the resonance frequency (f_o), marked as a $f_{optimum}$. Further investigation on $\eta_{cc_{max}}$ and ZVS at different operating frequencies in CC and CV modes with the experimental results has been done from the next paragraph.

At the time of charging in CC and CV modes, the voltage and current waveforms of the inverter and battery bank are observed. In CC mode, the waveforms are recorded for inverter output and battery bank, as shown in Fig. 7. Since the current is constant in CC mode, an effective load resistance R_{ac} will change only due to the voltage rise, which is less significant, as shown in Fig. 5(b). In CC mode, at a particular instant of time, R_{ac} is experimentally measured as 126 Ω [marked in Fig. 5(b)]. Since the electrical characteristics of the battery bank will change over the time, the battery bank is replaced by an equivalent resistive load of 126 Ω to maintain same R_{ac} for further experiment.

In Fig. 8(a), the variation of load phase angle obtained from (9) and measured from the experiment are shown for different operating frequencies when $R_{ac} = 126\ \Omega$. It can be observed from Fig. 8(a) that both the curves are following the same nature. It can also be seen that to increase the load phase angle of the system, operating frequency should be decreased from its resonance frequency. The plot of η_{cc} versus load phase angle obtained from (9) and (12), and measured from the experiment, is given in Fig. 8(b). From Fig. 8(b), an almost constant nature of η_{cc} is seen with variation in the load phase angle. However, in zoomed version, a parabolic nature is seen with an increase in load phase angle. Hence, it has a maximum efficiency point, which is about 15° from the calculation and 17° from the measurement.

At resonance frequency, the experimental waveforms of primary voltage (inverter output) and current are given in Fig. 9. In Fig. 9, undesirable notches (due to inappropriate ZVS), marked in the red circle are noticed in the primary voltage waveform, which can affect the system stability. An improved waveform (due to proper ZVS) of the primary voltage is recorded at 184.3 kHz frequency (measured $f_{optimum}$), which is about 17° of load phase angle, as shown in Fig. 10.

From Figs 8–10, it can be seen that to obtain a stable performance, load phase angle should be increased by decreasing the operating frequency to $f_{optimum}$. In this way, the system stability can be improved with a maximum efficiency for lower load resistance in CC mode.

In CV mode, the voltage and current waveforms of inverter output and battery bank are recorded at the end stage of CV mode for a charging current of 140 mA, as shown in

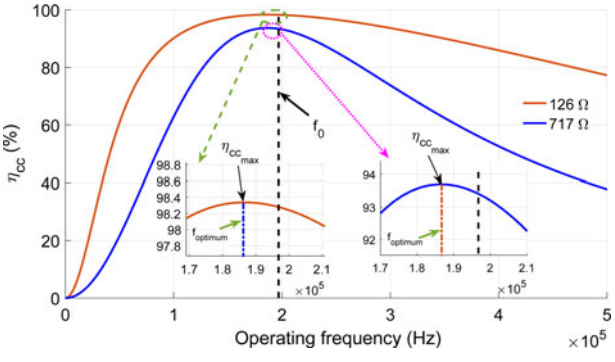

Fig. 6. Variation of calculated compensated coil efficiency w.r.t. different operating frequencies for $R_{ac} = 126\ \Omega$ and $717\ \Omega$.

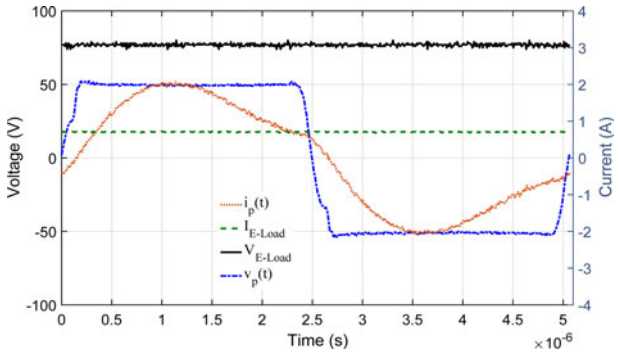

Fig. 7. Experimental waveforms in CC mode at the resonance frequency.

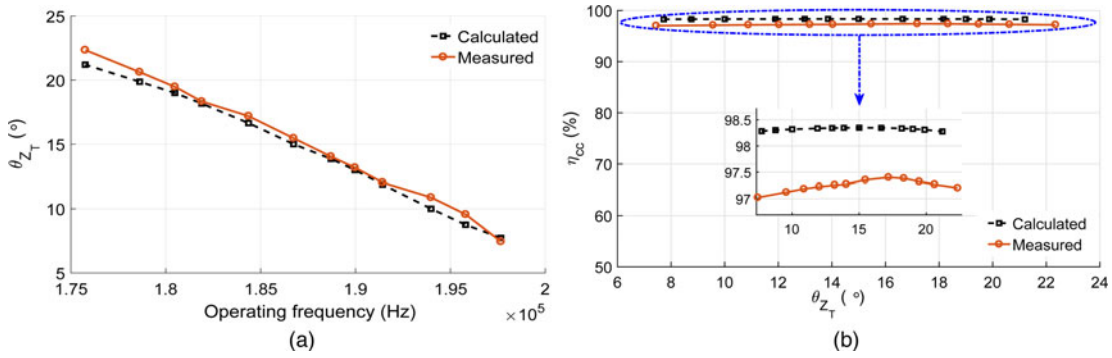

Fig. 8. Experimental results at $R_{ac} = 126\ \Omega$. (a) Load phase angle versus operating frequency and (b) compensated coil efficiency versus load phase angle.

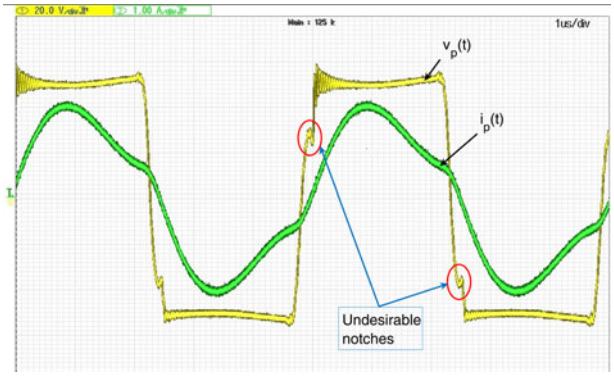

Fig. 9. Experimental waveforms of primary voltage and current (inverter output) at 197.6 kHz operating frequency (resonance frequency) and $R_{ac} = 126\ \Omega$.

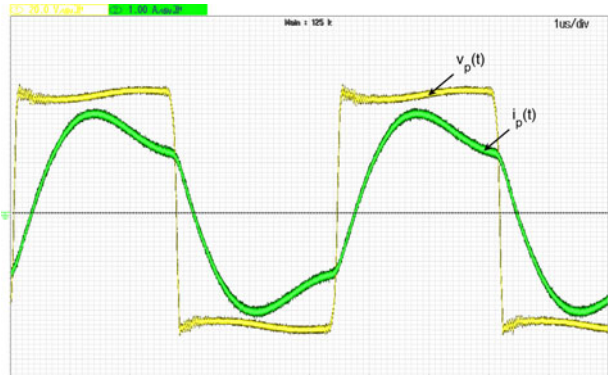

Fig. 10. Experimental waveforms of primary voltage and current (inverter output) at 184.3 kHz operating frequency and $R_{ac} = 126\ \Omega$.

Fig. 11. An effective load resistance R_{ac} is experimentally measured as 717 Ω [marked in Fig. 5(b)], which is higher than CC mode. To maintain R_{ac} (717 Ω), the battery bank is replaced with the resistive load for further experiment.

At $R_{ac} = 717\ \Omega$, again operating frequency is varied to maintain ZVS with maximum efficiency. The variation of load phase angle for different operating frequencies obtained from (9) and measured from the experiment when $R_{ac} = 717\ \Omega$ is plotted in Fig. 12(a), and the η_{cc} observed at each load phase angle calculated from (9) and (12) is given in Fig. 12(b). From Fig. 12(a), it can be examined that both the curves are following the same pattern. In CV mode, the waveform of inverter voltage is stable throughout the variation, even at the resonance frequency, as shown in Fig. 11. From

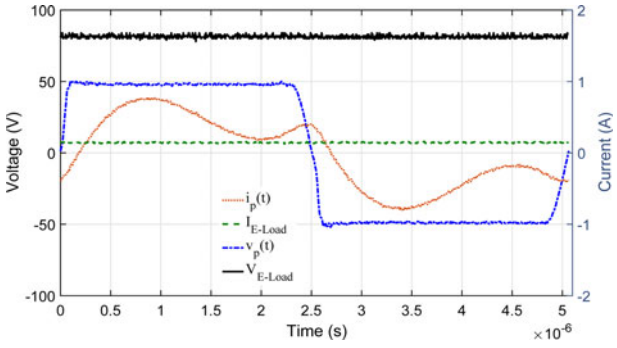

Fig. 11. Experimental waveforms in CV mode at the resonance frequency.

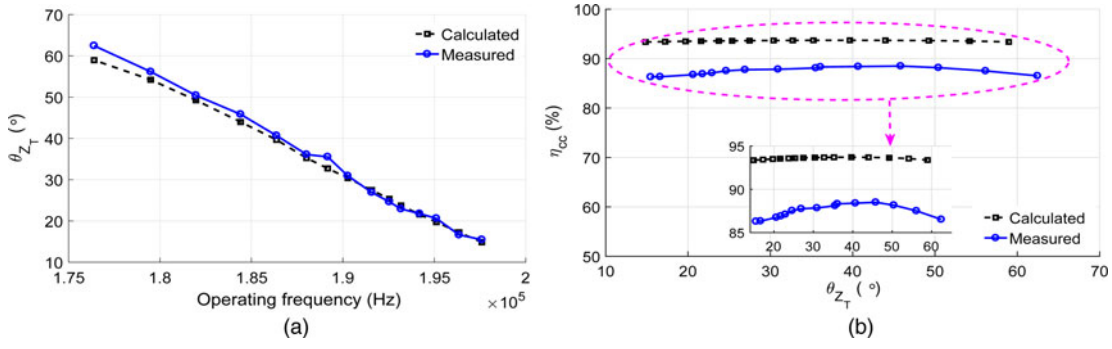

Fig. 12. Experimental results at $R_{ac} = 717\ \Omega$. (a) Load phase angle versus operating frequency and (b) compensated coil efficiency versus load phase angle.

Fig. 12(b), it is observed that the η_{cc} is maximum when load phase angle is about 40° (obtained at $f_{optimum} = 186.5$ kHz) from the calculation and about 45° (obtained at $f_{optimum} = 184.4$ kHz) from the measurement. In addition, a parabolic nature of the η_{cc} curve is noticed with an increase in the load phase angle.

From the above discussion, it can be noticed that, by controlling the load phase angle in both CC and CV modes, a stable performance and maximum efficiency can be achieved.

IV. CONCLUSION

An experimental analysis in open loop for the lead acid battery charging using the SP compensated CPT system is presented. Measured charging profile and the equivalent resistance profile of the lead acid battery bank are presented in CC and CV modes. Lower to higher variations in R_{ac} are observed during the charging process. An expression of optimum operating frequency is derived to get the maximum compensated coil efficiency during the load variation in charging process. An open-loop control is performed to ensure the system stability and maximum efficiency at obtained optimum operating frequency in CC and CV modes. From the experimental results and discussion, a suitable closed-loop robust controller can be implemented.

REFERENCES

[1] Covic, G.A.; Boys, J.T.: Modern trends in inductive power transfer for transportation applications. IEEE J. Emerg. Sel. Top. Power Electron., **1** (1) (2013), 28–41.

[2] Li, S.; Mi, C.C.: Wireless power transfer for electric vehicle applications. IEEE J. Emerg. Sel. Top. Power Electron., **3** (1) (2015), 4–17.

[3] Fisher, T.; Farley, K.; Gao, Y.; Bai, H.; Tse, Z.: Electric vehicle wireless charging technology: a state-of-the-art review of magnetic coupling systems. Wireless Power Transf., **3** (2) (2014), 87–96.

[4] Sallan, J.; Villa, J.L.: Optimal design of ICPT systems applied to electric vehicle battery charge. IEEE Trans. Power Electron., **56** (6) (2009), 2140–2149.

[5] Zheng, C., et al. High-efficiency contactless power transfer system for electric vehicle battery charging application, in 2013 IEEE Energy Conversion Congress and Exposition, Denver, CO, USA, 2013, 3243–3249.

[6] Joy, E.R.; Kushwaha, B.K.; Rituraj, G.; Kumar, P.: Analysis and comparison of four compensation topologies of contactless power transfer system, in 2015 4th Int. Conf. Electric Power Energy Conversion System (EPECS), Sharjah, UAE, 2015, 1–6.

[7] Monti, G.; Costanzo, A.; Mastri, F.; Mongiardo, M.: Optimal design of a wireless power transfer link using parallel and series resonators. Wireless Power Transf., **3** (2) (2016), 105–116.

[8] Aditya, K.; Williamson, S.S.: Comparative study of series-series and series-parallel compensation topologies for electric vehicle charging, in 2014 IEEE 23rd Int. Symp. Industrial Electronics (ISIE), Turkey, 2014, 426–430.

[9] Aditya, K.; Williamson, S.S.: Comparative study of series-series and series-parallel topology for long track EV charging application, in 2014 IEEE Transportation Electrification Conf. and Expo (ITEC), Dearborn, MI, USA, 2014, 1–5.

[10] Rituraj, G.; Joy, E.R.; Kushwaha, B.K.; Kumar, P.: Analysis and comparison of series-series and series-parallel topology of contactless power transfer systems, in 2014 IEEE Region 10 Conf. TENCON, Bangkok, Thailand, 2014, 1–6.

[11] Chao, Y.H.; Shieh, J.J.; Pan, C.T.; Shen, W.C.: A closed-form oriented compensator analysis for series-parallel loosely coupled inductive power transfer systems, in 2007 IEEE Power Electronic Specialists Conf. (PESC), Orlando, FL, USA, 2007, 1215–1220.

[12] Liu, N.; Habetler, T.G.: Design of a universal inductive charger for multiple electric vehicle models. IEEE Trans. Power Electron., **30** (11) (2015), 6378–6390.

[13] Jiang, B.; Wang, J.G.; Chen, L.J.; Wang, B.; Wang, Q.: A efficient control method for series-parallel CPT system, in 2014 33rd Chinese Control Conf. (CCC), Nanjing, China, 2014, 3500–3504.

[14] Huang, S.J.; Li, Y.J.; Huang, B.G.; Shen, W.C.: Contactless energy-transfer system design for lithium iron phosphate battery-charging circuits, in 2013 IEEE 10th Int. Conf. Power Electronics Drive System (PEDS), Kitakyushu, Japan, 2013, 217–220.

[15] Zheng, C., et al. High-Efficiency contactless power transfer system for electric vehicle battery charging application. IEEE J. Emerg. Sel. Top. Power Electron., **3** (1) (2015), 65–74.

[16] Buja, G.; Bertoluzzo, M.; Mude, K.N.: Design and experimentation of WPT charger for electric city Car. IEEE Trans. Ind. Electron., **62** (12) (2015), 7436–7447.

[17] Wang, C.S.; Covic, G.A.; Stielau, O.H.: Power transfer capability and bifurcation phenomena of loosely coupled inductive power transfer systems. IEEE Trans. Ind. Electron., **51** (1) (2004), 148–157.

[18] Kushwaha, B.K.; Rituraj, G.; Kumar, P.: Mathematical model of series-parallel compensation for contactless power transfer system, in 2016 IEEE Int. Power Electronics and Motion Control Conf. (PEMC), Varna, Bulgaria, 2016, 1020–1025.

Gautam Rituraj received the B.Tech. degree in Electrical Engineering from the Uttar Pradesh Technical University, Lucknow, India, in 2012. He is currently pursuing the Ph.D. degree with the Department of Electronics and Electrical Engineering, IIT Guwahati, Guwahati, India. His current research interests include the analysis and design of stationary wireless power transfer systems and developing the power electronic circuits for electric vehicle charging.

Brijesh Kumar Kushwaha received the B.Tech. degree in Electronics and Communication Engineering from the Uttar Pradesh Technical University, Lucknow, India, in 2010, and the M.Tech. degree in Power Electronics and Application Specified Integrated Circuit Design from the Motilal Nehru National Institute of Technology, Allahabad, India, in 2012. He is currently pursuing the Ph.D. degree with IIT Guwahati, Guwahati, India. His current research interests include the modeling of wireless power transfer systems, magnetic field theory, and power electronics.

Praveen Kumar received the B.Tech. degree in Electrical Engineering from the National Institute of Technology, Hamirpur, India, in 1998, the M.Tech. degree in Energy System from the IIT, Delhi, India, in 2000, and the Ph.D. degree from the Delft University of Technology, Delft, The Netherlands. He is currently an Associate Professor with IIT Guwahati, Guwahati, India. He was a Team Leader of Hybrid Systems with Drive Trains Innovation, Eindhoven, The Netherlands. His current research interests include optimization of electrical motors and drives, hybrid and electric vehicles, smart grid, and wireless charging of electric vehicles.